Flow Transport and Inclusion Motion in Steel Continuous-Casting Mold under Submerged Entry Nozzle Clogging Condition

LIFENG ZHANG, YUFENG WANG, and XIANGJUN ZUO

Clogging of the submerged entry nozzle (SEN) is a serious problem during the continuous casting of steel, due to its influence on the casting operations and product quality. Fluid-flow-related phenomena in the continuous casting mold region with the SEN clogging are investigated in the current article, including the quantitative evaluation of inclusion removal, slag entrainment, heat transfer, and the prediction of breakouts. The calculations indicate that, in order to accurately simulate the fluid flow in the mold region, the SEN should be connected with the mold region and the two should be calculated together. In addition, the whole mold region has to be calculated. Clogging at the SEN at one side induces asymmetrical jets from the two outports; thus, the fluid flow in the mold is asymmetrical. In addition, more inclusions are carried by the flow to the top surface of the nonclogged side, and the slab at the nonclogged side has a lower quality. With SEN one-sided clogging, inclusions travel a much larger distance, on average, before they escape from the top or move to the bottom. The overall inclusion entrainment fraction from the entire top surface for inclusions of any size is less than 10 pct. A higher turbulence energy and a larger surface velocity induce more inclusion entrainment from the top surface. Smaller inclusions are more easily entrained into the steel than are larger ones. More $>200\text{-}\mu m$ inclusions can be entrained into the molten steel from the top slag with SEN clogging than without clogging. The SEN one-sided clogging generates an asymmetrical temperature distribution in the mold; it also generates temperatures higher than the liquidus temperature at some locations of the solidified shell, which increases the risk of breakouts. The SEN clogging should be minimized in order to achieve a uniform steel cleanliness, a cleaner steel, and a safe continuous casting operation.

I. INTRODUCTION

CLOGGING of the submerged entry nozzle (SEN) is a serious problem during the continuous casting of steel, due to its influence on the casting operations and product quality. The jet characteristics and flow pattern are changed near the outports of the SEN, which results in asymmetric flow and abnormal temperature distribution in the mold. These phenomena lead to the entrapment of inclusions onto the solidified shell, the entrainment of top liquid slag, and even breakouts.

There have been many studies of the issue of the SEN clogging.[1–9] Clogging can be classified into four general types by its different origins:[6–8] the agglomeration of deoxidation products, solid steel buildup, the agglomeration of complex oxides, and buildup from reaction products. Industrial observations indicate that the clogging materials at the SEN port area have a combined chemistry that is indicative of mold flux and deoxidation inclusions. It is possible that mold flux is drawn into the top of the port due to the recirculation flow pattern in the upper part of the mold and due to tendency of the liquid flux to coat the nozzle.[6,10,11] However, the primary cause of SEN clogging is the deposition of the solid inclusions already present in the steel,[12] especially the alumina inclusions, which attach easily to the hot refractory, due to the effect of the surface energy.[13–15] It has been reported that ~10 pct of alumina inclusions that leave the tundish adhere to the SEN walls.[16]

In recent years, mathematical models were developed to investigate the SEN clogging.[17,18] The optimum gas injection rate at the SEN for preventing SEN clogging during steel continuous casting was obtained by numerical calculation.[19,20] The shear stress magnitudes on the SEN walls were predicted using mathematical models, in order to design a suitable SEN and decrease the attachment of inclusions to the lining refractory.[21,22] However, there has been little research using fluid flow simulation that quantitatively investigates the effect of the SEN clogging on inclusion removal, slag entrainment, breakout, etc. The use of mathematical modeling for investigating the effect of the SEN clogging on steel quality is very convenient; this is because, while SEN clogging cannot be easily and exactly adjusted in real industrial continuous casting, mathematical modeling can be used to achieve this adjustment.

LIFENG ZHANG, Assistant Professor, YUFENG WANG and XIANGJUN ZUO, Ph.D. Graduate Students, are with the Department of Material Sciences and Engineering, Missouri University of Science and Technology, Rolla, MO 65409-0330. Contact e-mail: zhanglife@mst.edu

In the current article, fluid-flow-related phenomena due to SEN clogging were investigated, including velocity distribution, inclusion entrapment, slag entrainment, heat transfer, and breakout possibilities. The entrapment positions of inclusions on SEN walls were predicted.

II. MATHEMATICAL FORMULATION AND COMPUTATIONAL CONDITIONS

The three-dimensional (3-D) single-phase steady turbulent fluid flow in the SEN and continuous-casting mold was modeled by calculating the continuity equation and Navier–Stokes equations, using standard equations for turbulent energy and its dissipation rate. The distribution of temperature and the dissipation of superheat in the molten steel strand were predicted by solving an additional heat transport equation. Detailed equations can be found elsewhere.[23–25] The equations were solved using the commercial code FLUENT;[26] for this research, the residual was set below 10^{-6}.

In the current article, fluid flow in a full mold region, including the tundish bottom well, the upper nozzle, the slide gates, the SEN, the mold, and the vertical length of the caster, was calculated. The inlet is the tundish bottom well. The whole computational domain, including the SEN and the continuous-casting mold region, was divided into 370,000 cells, and the mesh on each side of the full mold was completely symmetrical. The geometry and the mesh system are shown in Figure 1. The main dimensions and parameters for the continuous-casting process in the current study are listed in Table I.

The trajectory of each inclusion particle was then calculated from the computed velocity equation using the Lagrangian–Lagrangian approach,[20] which considers the balance between drag, buoyancy forces, and other interfacial forces:

$$\frac{du_{pi}}{dt} = \frac{18\mu}{\rho_P d_P^2} \frac{C_D \mathrm{Re}_P}{24} (u_i - u_{pi}) + \frac{\rho_P - \rho}{\rho} g_i$$
$$+ \frac{1}{2}\frac{\rho}{\rho_P}\frac{d}{d_t}(u_i - u_{pi}) + \frac{\rho}{\rho_P}u_i\frac{\partial u_i}{\partial x_i} \qquad [1]$$

The drag force coefficient is given by

$$C_D = \frac{24}{\mathrm{Re}_P}\left(1 + 0.186\mathrm{Re}_P^{0.6529}\right) \qquad [2]$$

The first term in Eq. [1] is the drag force per unit particle mass, the second term is the gravitational force, the third term is the "virtual mass" force accelerating the fluid surrounding the particle,[27] and the fourth term is the force stemming from the pressure gradient in the fluid.

To incorporate the "stochastic" effect of turbulent fluctuations on the particle motion, this work uses the "random walk" model.[26] In this model, particle velocity fluctuations are based on a Gaussian-distributed random number chosen according to the local turbulence kinetic energy. The random number is changed, thus producing a new instantaneous velocity fluctuation,
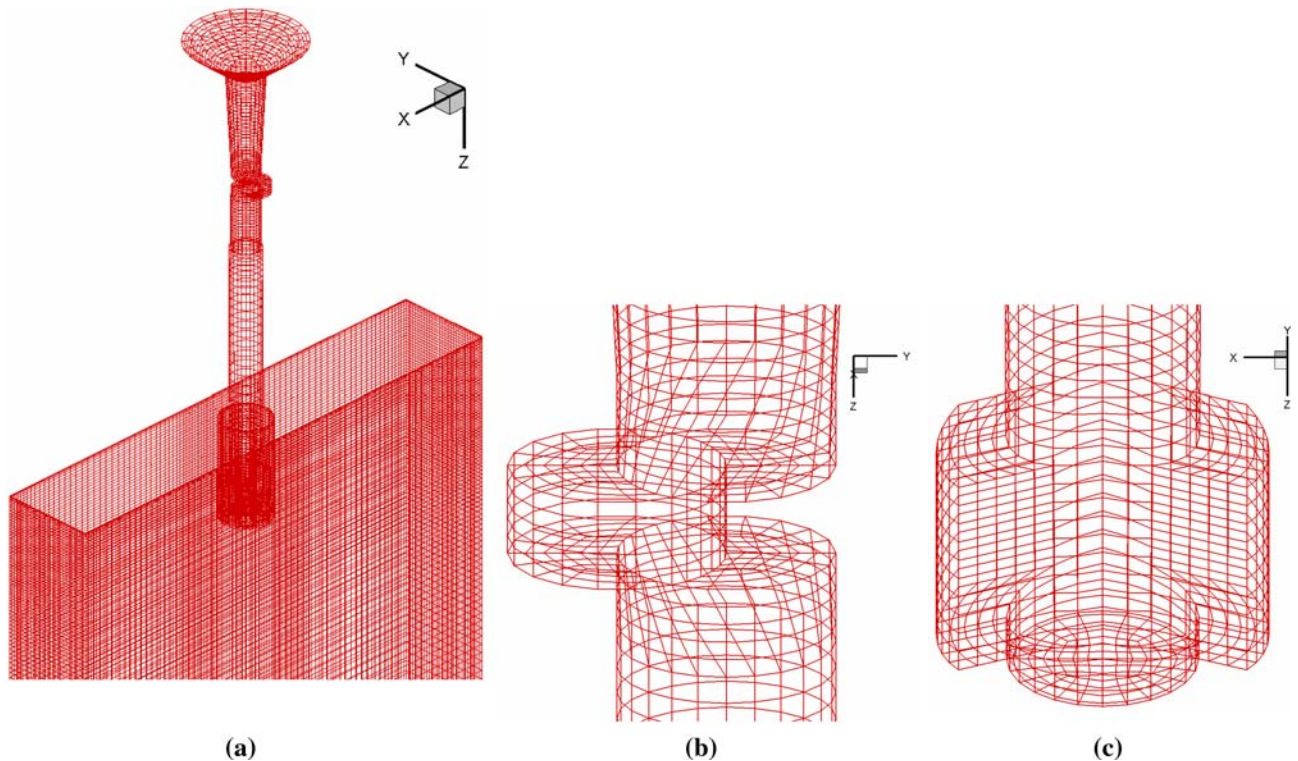

Fig. 1—Computational domain and mesh system: (*a*) SEN and mold, (*b*) slide gate, and (*c*) outport.

Table I. Main Dimensions and Parameters

Parameter	Value	Parameter	Value
SEN bore diameter	70 mm	Viscosity of liquid steel	0.0067 kg/m·s
Port width × height	65 × 80 mm	Density of liquid steel	7020 kg/m^3
Mold cross section	1300 × 250 mm	Thermal conductivity	41 w/m·k
Mold working length	800 mm	Density of inclusions	5000 kg/m^3
Vertical length of the mold region	2.55 m	Number of inclusions for each simulation	20,000
Port angle	15 deg down	Casting temperature	1818 K
Up nozzle length	323 mm	Liquidus temperature	1788 K
Total nozzle length	1229 mm	Steel thermal expansion coefficient	1×10^{-4} 1/K
Slide-gate orientation	90 deg	Diameter of the tundish bottom well	300 mm
Slide-gate opening	50 pct	Inlet velocity	0.102 m/s
SEN submerged depth	150 mm	Inlet kinetic energy	0.001066 m^2/s^2
Casting speed	1.2 m/min	Inlet dissipation rate	0.000256 m^2/s^3
		Heat loss at the top surface	15,000 W/m^2

at a frequency equal to the characteristic lifetime of the eddy. The instantaneous fluid velocity is then given by

$$u = \bar{u} + u' \qquad [3]$$

$$u' = \xi\sqrt{\overline{u'^2}} = \xi\sqrt{2k/3} \qquad [4]$$

As a boundary condition, it is assumed that, once the inclusion touches the wall, it will adhere to the SEN. This is a crude preliminary approximation that is being investigated further as part of this project. The entrapment of particles onto the wall and the solidifying shell is very complex; it has received well-deserved attention in recent work.[28–30] Furthermore, the entrapment of inclusions to the SEN lining refractory should be much easier than their entrapment to the solidified shell, since the surface energy between the inclusions and the lining refractory is very different from that between the inclusions and the solidifying front. In addition, the surface of the lining refractory is very rough.

III. TREATMENT OF COMPUTATIONAL DOMAIN

A. Connection between SEN and Mold Region

The flow pattern and jet angle near the SEN outports strongly influence the flow field and thermal dissipation in the mold region. For the simulation of fluid-flow-related phenomena in the nozzle and mold region, the following three approaches can be (and have been) used.

(a) In approach I, the slide gate and SEN are ignored; the inlet of the mold region is the SEN outport. The inlet jet angle is assumed to be the same as the downward angle of the SEN outport,[31,32] or as measured by a water model.[33] The value of the inlet velocity is estimated from the flow rate.
(b) In approach II, the fluid flow in the SEN is calculated first. Then the velocity profile and the turbulent energy and its dissipation rate at the SEN outport are imported as the inlet conditions for the

mold region. The fluid flow in the mold region is then calculated.[7,34–37]
(c) In approach III, the SEN and the mold region are connected together and the fluid flows both in the SEN and the mold region are calculated simultaneously.

It has been reported that the slide gate generates a swirl flow at the SEN outport,[16,38] and the actual jet downward angle is usually larger than the downward angle of the SEN outports.[39,40] Approach I ignores these phenomena. With approach II, there is a problem in setting the backflow condition at the SEN outports. The backflow condition affects the final velocity and the turbulent properties at the SEN outports and, therefore, also affects the fluid flow in the mold region. Approach III is the most accurate method; it has been rarely used, however, due to the difficulty of convergence.

The jet characteristics at the SEN outports using approaches II and III are shown in Figure 2 and Table II; the definition of the jet characteristics is included in Reference 34. Quantitatively, the jet strength is defined by the outflow from the ports. The following conclusions were obtained.

(a) The jet downward angle is larger than the SEN outport angle. As shown in Figure 2, the outport has a 15-deg downward angle, but the downward angle of the jet is >25 deg.
(b) Approach II has a larger jet angle and a higher jet speed and jet turbulent energy and its dissipation rate than those of approach III.
(c) The backflow situation at the SEN outports is different for approach II as compared to approach III. The backflow rate for approach II is approximately 7.2 pct of the total flow rate; for approach III, this value is 5.9 pct. The backflow turbulent energy and its dissipation rate in approach II are more than 10 times larger than those in approach III.

Thus, in order to accurately simulate the fluid flow in the mold region, the SEN should be connected with the mold region and the two should be calculated together. All the later simulations in the current article use approach III.
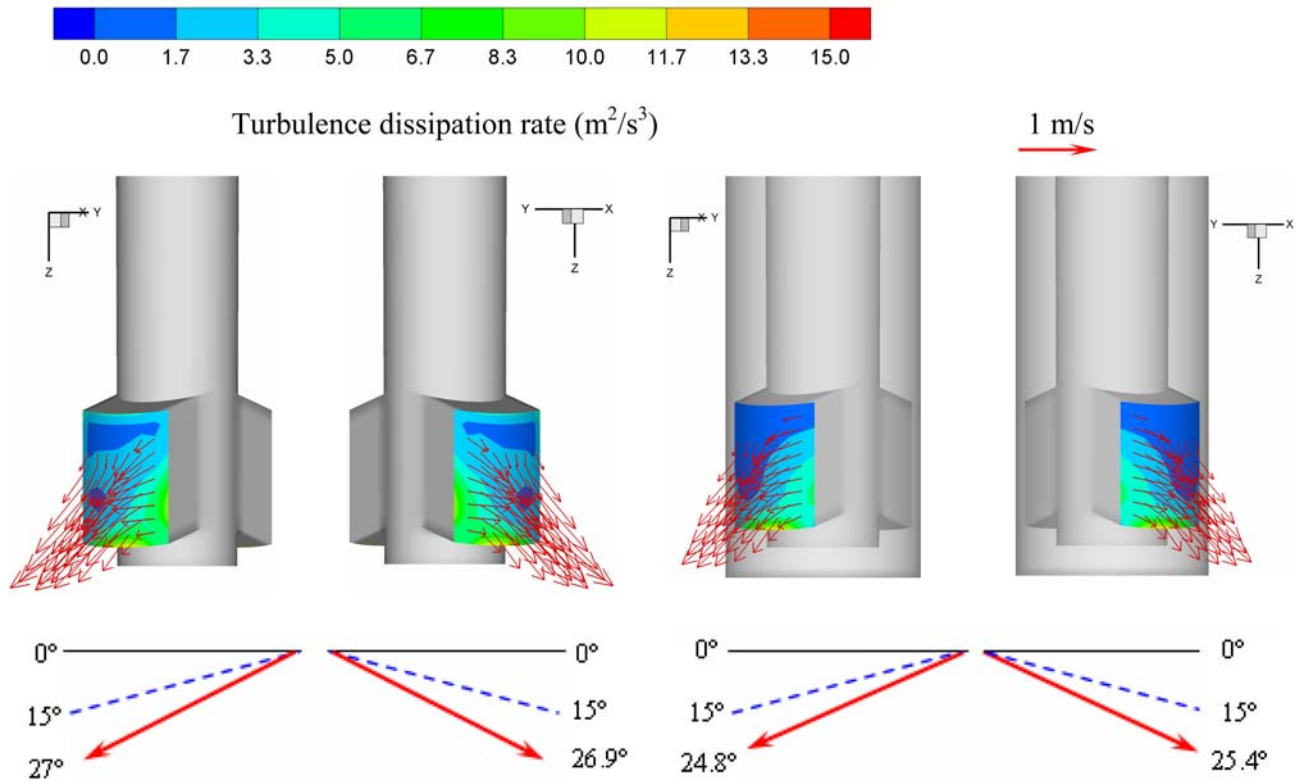
Fig. 2—Characteristics of jet at SEN outports (dashed angle is outport structure angle; solid angle is jet angle at SEN outports): (*a*) approach II and (*b*) approach III.

Table II.   Jet Characteristics at SEN Outports with Approaches II and III

| | Approach II | | | | Approach III | | | |
| | Left | | Right | | Left | | Right | |
Parameters	Outflow	Backflow	Outflow	Backflow	Outflow	Backflow	Outflow	Backflow
V_x (m/s)	−0.934	0.266	0.935	−0.264	−0.856	0.152	0.840	−0.178
V_y (m/s)	0.0138	0.00857	0.0137	0.00835	0.00686	0.0228	0.00172	−0.00501
V_z (m/s)	0.476	−0.00156	0.474	−0.00115	0.396	0.133	0.399	0.154
$\overline{V}$ (m/s)	1.101	0.292	1.102	0.291	0.974	0.134	0.961	0.260
$\overline{k}$ (m²/s²)	0.165	0.126	0.166	0.127	0.136	0.0163	0.133	0.0184
$\overline{\varepsilon}$ (m²/s³)	3.177	2.456	3.184	2.471	2.186	0.130	2.132	0.142
Q (m³/s)	0.0234	0.00191	0.0234	0.0019	0.0247	0.00156	0.0244	0.00153

B. *Half Mold Calculation and Full Mold Calculation*

In past investigations,[41,42] the fluid flow in a half mold region was calculated by assuming the symmetrical fluid flow pattern in the whole mold region. However, if clogging at the SEN occurs, the fluid flow in the mold region will be asymmetrical.

The difference between the half mold calculation and the full mold calculation is compared in Figure 3. The flow pattern in Figure 3(a) is the simulation of the half mold without SEN clogging and with a mirror to another half mold, thus completed symmetrical. The velocity distribution in a full mold without clogging is

shown in Figure 3(b); this indicates an asymmetrical flow pattern. In the current simulation, the residual of the solution below 10^{-6} has been achieved, which assures a good numerical convergence. This slightly asymmetrical flow pattern is to be expected, since there is no constraint to maintaining the centerline velocity in an exactly vertical mode.

Based on this discussion, in the later sections of the current article, the mold is connected with the nozzle system, including the tundish bottom well, upper nozzle, slide gate, and SEN, and the fluid flow in the full mold region is calculated.
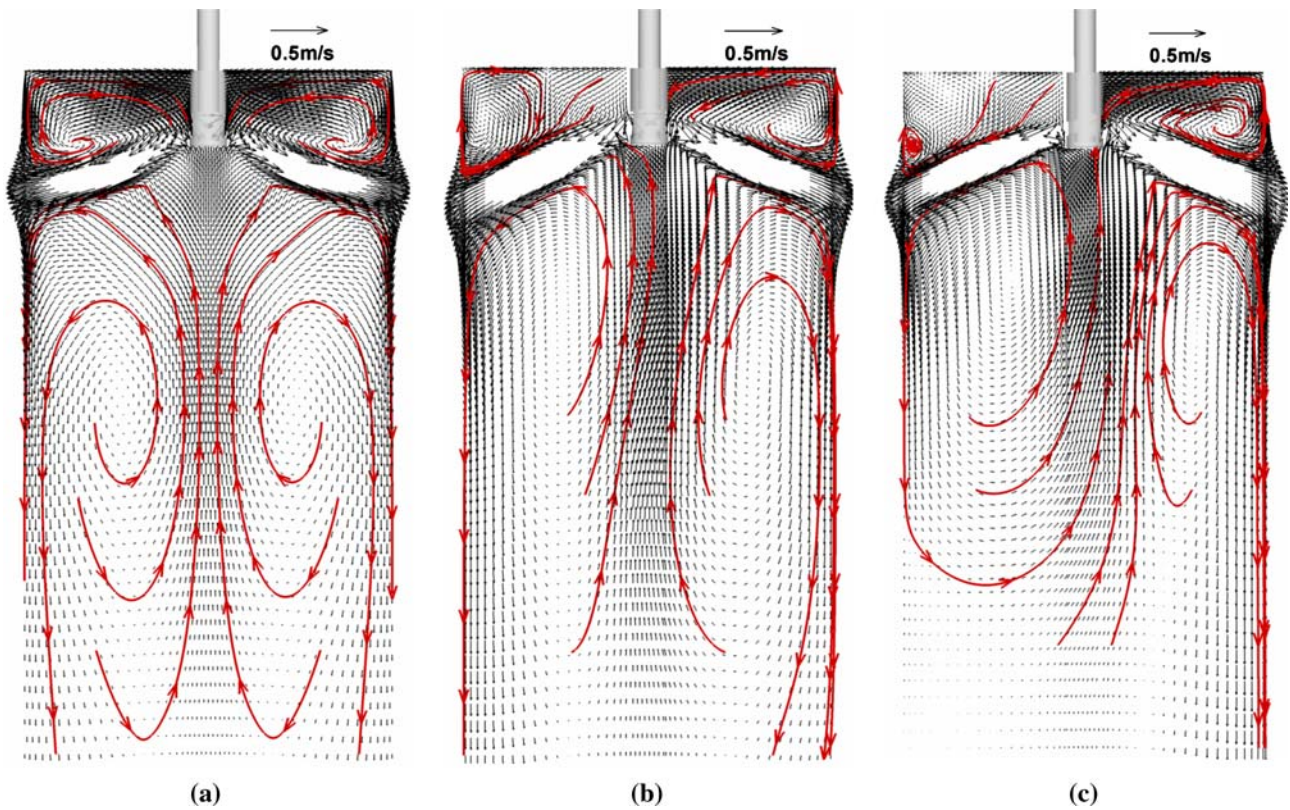
Fig. 3—Fluid flow pattern in the mold region: (a) mirror of half mold calculation, (b) full mold calculation without clogging, and (c) full mold calculation with clogging at SEN left outport.
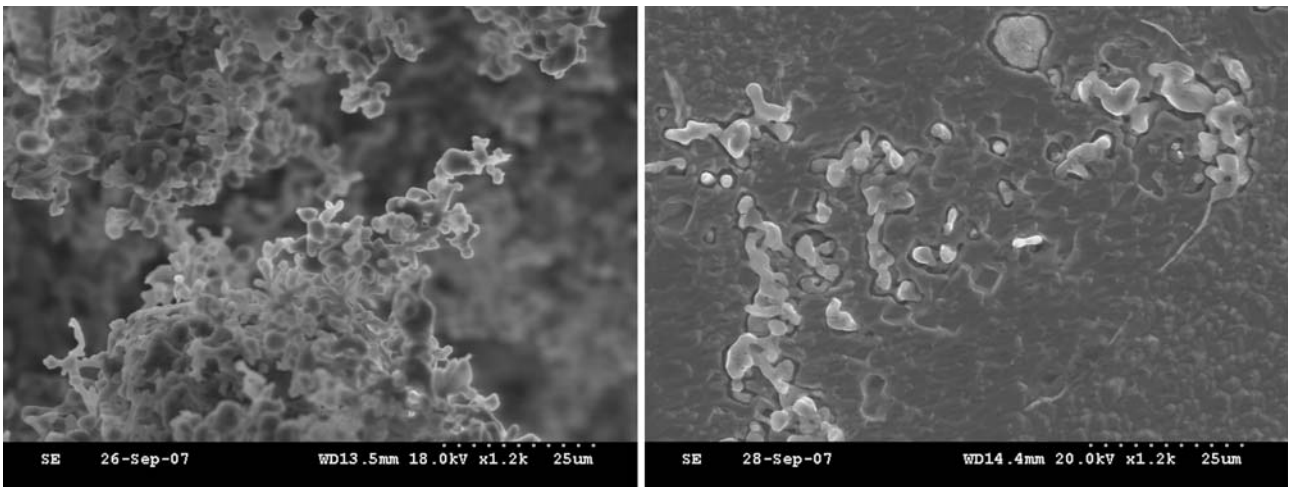

Fig. 4—Alumina particles clogged at SEN.[9] (At left are Al₂O₃ inclusions attached on SEN inner wall; at right are inclusions and frozen steel attached on SEN inner wall).

IV. EFFECT OF SEN CLOGGING ON FLUID FLOW AND INCLUSION MOTION IN THE MOLD REGION

A. Prediction of Clogging Position

Clogging occurs in two steps: the transport of the inclusions to the SEN wall and the adhesion of inclusions to the wall. At the end of the secondary refining of Al-killed steels, most alumina inclusions and the newly generated inclusions due to reoxidation are 2 to 10 μm;[43] these small inclusions may form big clusters. The typical inclusions that adhere to the wall of the SEN are shown in Figure 4,[9] which indicates a typical clogging inclusion size of 5 to 10 μm and big clusters. This figure also indicates that frozen steel is one of the main clogging materials.
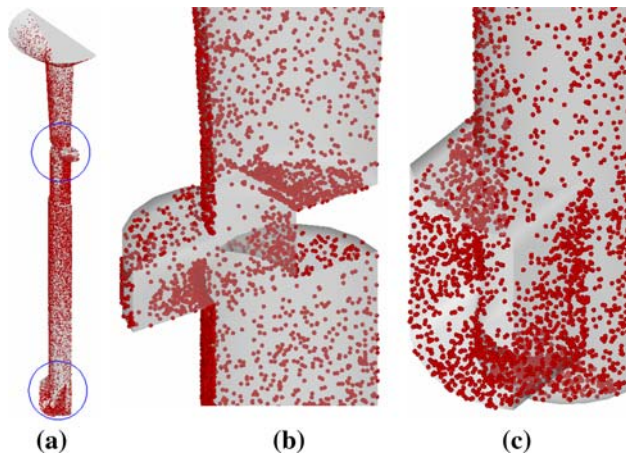
Fig. 5—Inclusion entrapment locations at SEN walls in current calculation: (*a*) whole SEN, (*b*) clogged near the slide gate, and (*c*) clogged near the SEN outport.
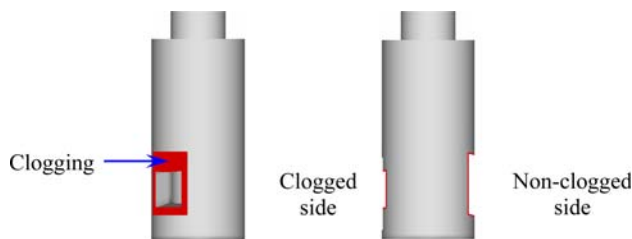

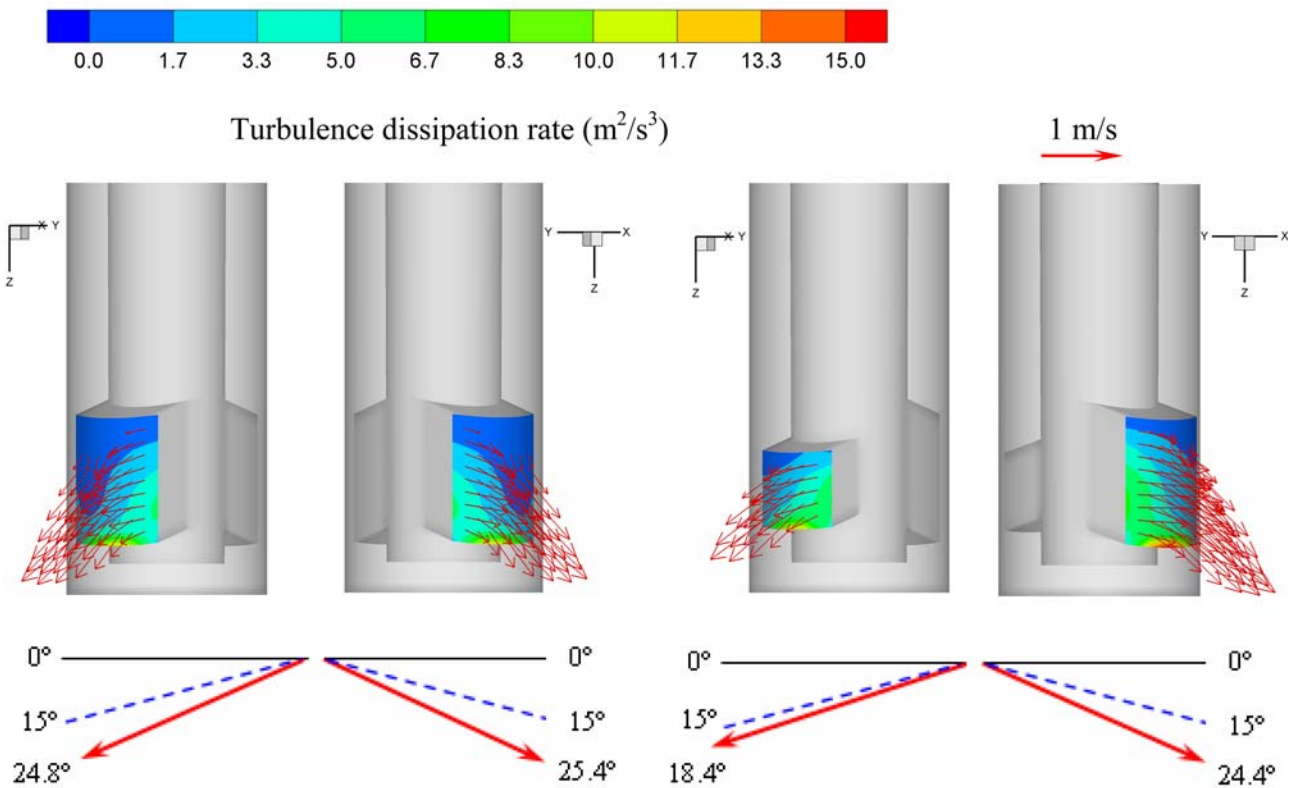Fig. 6—Assumed clogging condition at SEN outports.

In the current simulation, 20,000 inclusions with a diameter of 5 μm were injected into the domain through the tundish bottom well. Inclusion final entrapment positions on the SEN inner walls are shown in Figure 5(a). Inclusions tend to accumulate and adhere to the wall near the slide gate and the outports, especially to the inner well wall below the slide gate and the bottom and the lower side of the outports, as shown in Figures 5(b) and (c).

According to the calculated inclusion entrapment location, and in order to quantitatively investigate the heat transfer, inclusion motion, and inclusion removal in the mold, the following two cases are calculated.

(a) In case I, nonclogging, there is no clogging at the SEN.
(b) In case II, clogging, a 50 pct area reduction is assumed to occur at the left outport of the SEN (clogged side), and no clogging is assumed at the right outport (nonclogged side), as shown in Figure 6.

B. *Fluid Flow in the SEN and the Mold Region*

The jet characteristics at the SEN outports in these two cases are compared, as is shown in Figure 7 and Table III. Due to the reduction of the outport area at the clogged side, the velocity, turbulence dissipation rate, and average jet angle are different from those found at the nonclogged side. The jet angle at the clogging side is 18.4 deg; it is 24.4 deg at the nonclogged side. Without

Fig. 7—Turbulence dissipation rate, velocity, and outflow angle at SEN outport. Outports under (*a*) nonclogged and (*b*) left-side clogged conditions. (Dashed angle is outport structure angle; solid angle is jet angle at SEN outport).

Table III. Jet Characteristics at SEN Outports with NonClogging and One-Sided Clogging

| Parameters | Case I: Nonclogging | | | | Case II: One-Sided Clogging | | | |
| | Left | | Right | | Left | | Right | |
	Outflow	Backflow	Outflow	Backflow	Outflow	Backflow	Outflow	Backflow
V_x (m/s)	−0.856	0.152	0.840	−0.178	−1.001	0.164	1.002	−0.171
V_y (m/s)	0.00686	0.0228	0.00172	−0.00501	0.00405	−0.0197	0.00735	0.0273
V_z (m/s)	0.396	0.133	0.399	0.154	0.333	−0.0317	0.454	0.190
$\overline{V}$ (m/s)	0.974	0.134	0.961	0.260	1.085	0.231	1.142	0.281
$\overline{k}$ (m^2/s^2)	0.136	0.0163	0.133	0.0184	0.163	0.0254	0.176	0.0260
$\overline{\varepsilon}$ (m^2/s^3)	2.186	0.130	2.132	0.142	3.835	0.442	3.097	0.256
Q (m^3/s)	0.0247	0.00156	0.0244	0.00153	0.0132	0.000254	0.0312	0.00110

SEN clogging, the jet angle is approximately 25 deg at both sides. The flow rate decreases to 0.0132 m^3/s at the clogged side and increases to 0.0312 m^3/s at the nonclogged side. When the clogging occurs, the jet angle is changed and the flow rate is reduced; the flow rate at the nonclogged side, however, increases. Hence, the liquid steel moves from the clogged side to the nonclogged side, which results in an obvious asymmetry in the mold. At the clogged side, the backflow rate is very small.

The distribution of the velocity vector and the streamlines for these two cases are shown in Figures 3 and 8. Clogging change the flow pattern in the SEN and in the jet characteristics exiting the ports and, therefore, changes the fluid flow pattern in the mold region, as is shown in Figures 3(c) and 8(b).

C. Inclusion Motion and Removal

In order to calculate the inclusion motion, removal, and entrapment in the mold region, 20,000 inclusions,
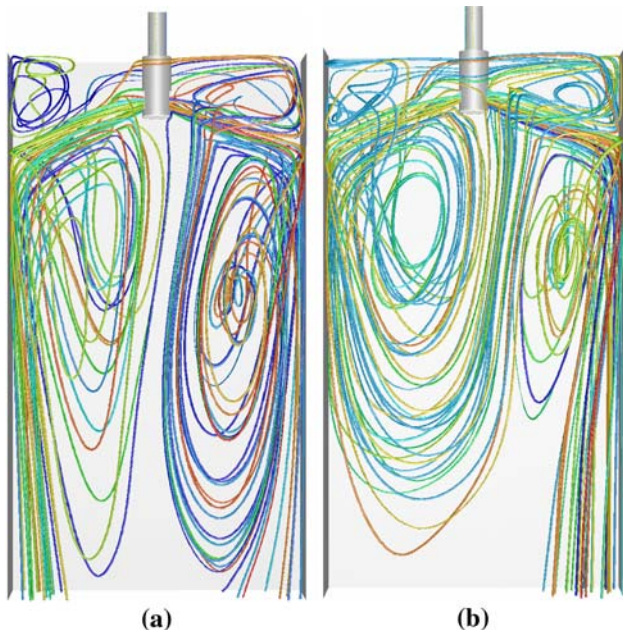

Fig. 8—3-D streamlines under different conditions: (a) nonclogged and (b) clogged at the SEN left outport.

each with a diameter of 50 μm, were injected into the SEN from the top over a 2-second time period. The inclusion locations at different times are shown in Figure 9. Inclusions reach the bottom of the liquid pool much more easily on the nonclogged side.

The calculated entrapment location of the inclusions on the top and the bottom of the mold region is shown in Figure 10. With clogging, the inclusions tend to be removed at the top surface of the nonclogged side. At the bottom of the liquid pool, more inclusions enter the nonclogged side, which hints a lower product quality there.

In order to quantitatively investigate the inclusion removal in the continuous-casting mold, two boundary conditions for inclusions at a solidified shell (wide faces and narrow faces) are considered: (1) a trap boundary condition, in which inclusions that once touch the shell are entrapped and (2) a reflection boundary condition, in which inclusions are totally bounced back if they touch the shell. The fraction of inclusions removed to the top surface by these two boundary conditions is shown in Figure 11. The real removal fraction of inclusions should lie between these two cases. Larger inclusions were easily removed and the removal fraction increases slightly if clogging occurs. With the trap boundary condition, only <10 pct of the inclusions were removed to the top surface, even for inclusions as large as 300 μm. Only <3 pct of the 50-μm inclusions were removed to the top surface. The typical trajectories of the inclusions are shown in Figure 12.

Under the reflection boundary condition, the mean path length and the mean residence time of 1000 inclusions of each size are shown in Figure 13. Inclusions were randomly injected into the SEN at the meniscus height. The following three conclusions were obtained.

(a) Both the path length and the residence time of small inclusions are larger than those of large inclusions.
(b) The path length of inclusions is far larger than the mold length (2.55 m), which hints at the recirculation and the random walk of inclusions in the mold.
(c) With SEN one-sided clogging, inclusions travel longer before escaping from the top or entering the bottom than they do in the nonclogging case.
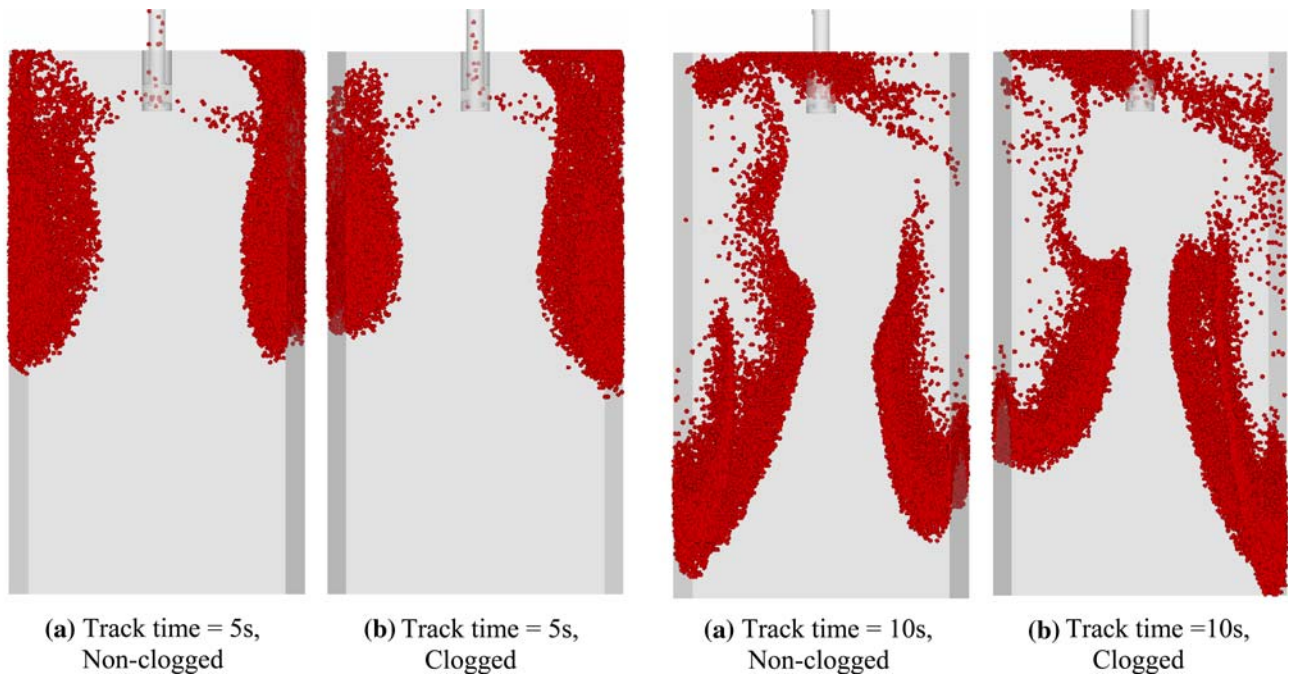
(a) Track time = 5s, Non-clogged **(b) Track time = 5s, Clogged** **(a) Track time = 10s, Non-clogged** **(b) Track time =10s, Clogged**

Fig. 9—Location of 50-μm inclusions at different time shots after injection from SEN.

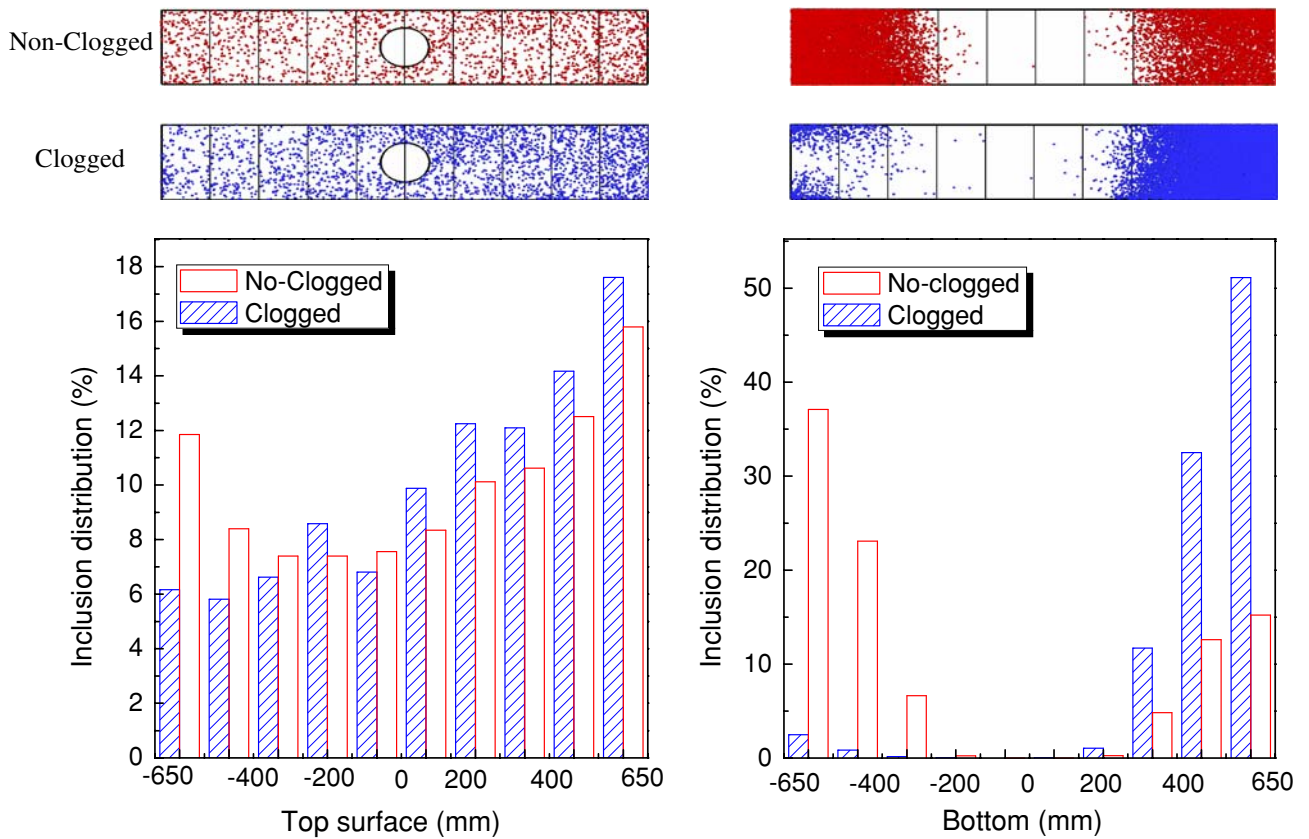Fig. 10—Distribution of 50-μm inclusions on the top and bottom of the mold region (2.55-m long).

D. Slag Entrainment (Particle Re-Entrainment from Top Surface)

The calculated entrainment fractions of 100-μm inclusions into the steel from the top surface are shown

in Figure 14. With the condition of the SEN left outport 50 pct clogging, the overall entrainment fraction from the entire top surface of the 100-μm inclusions is approximately 6 pct. The entrainment fraction at the

nonclogged side is much higher than it is on the clogged side, which agrees well with the water model observation,[44] as shown in Figure 14. Slag entrainment is related to the local turbulence energy near the top surface, as shown in Figures 14 and 15. The turbulence energy at the nonclogged side is higher than it is at the clogged side. In addition to the turbulence energy, slag entrainment may also be affected by the surface velocity, as shown in Figure 15. A higher turbulence energy and surface velocity induce more slag entrainment.
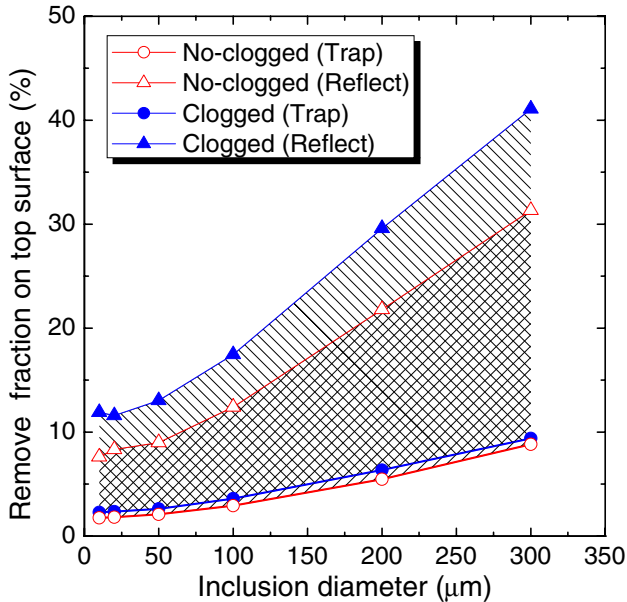
Fig. 11—Inclusion removal fraction to the top surface under different boundary conditions at wide and narrow faces of the mold.

The overall entrainment fraction at the entire top surface as a function of inclusion size is shown in Figure 16, which indicates the following.

(a) The overall entrainment for any size inclusion is less than 10 pct.
(b) Smaller inclusions are entrained more easily into the steel than are larger ones, due to the smaller buoyancy force of the smaller inclusions.
(c) The <200-μm inclusions are more easily entrained into the steel without SEN clogging than with SEN clogging, while the situation is the opposite for inclusions larger than 200 μm.
(d) For >200-μm inclusions, the buoyancy force dominates their motion; for <200-μm inclusions, the inertial force (fluid drag force) dominates.

E. *Heat Transfer and Prediction of Possible Breakout Zone*

Delivering superheat to the shell can significantly influence steel solidification. The following two cases are calculated.

(a) In case A, there is no clogging at the SEN. The temperature at the wide and narrow faces is fixed to the steel liquidus temperature. The temperature distribution inside the mold and the heat fluxes at the wide and narrow faces are then calculated.
(b) In case B, there is clogging of 50 pct of the area at the SEN left outport. The heat flux at the wide and narrow faces is fixed at the value calculated from case A. The temperature distribution inside the mold and at the wide and narrow faces is then calculated.
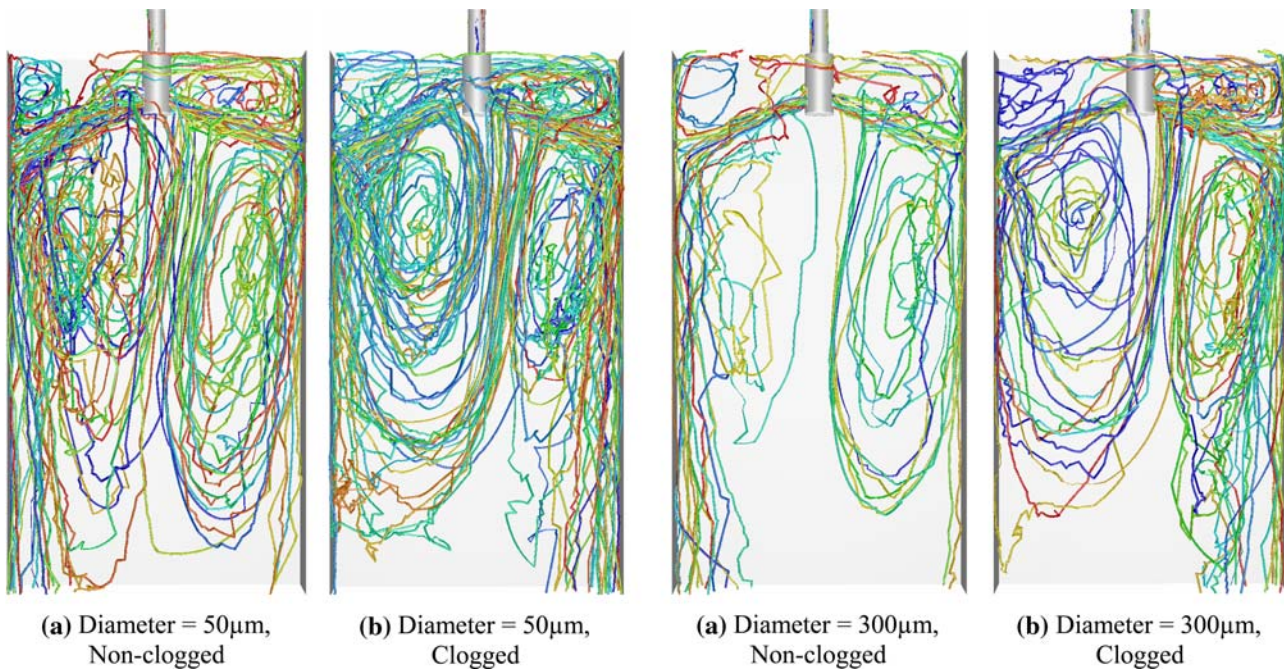

(a) Diameter = 50μm, Non-clogged

(b) Diameter = 50μm, Clogged

(a) Diameter = 300μm, Non-clogged

(b) Diameter = 300μm, Clogged
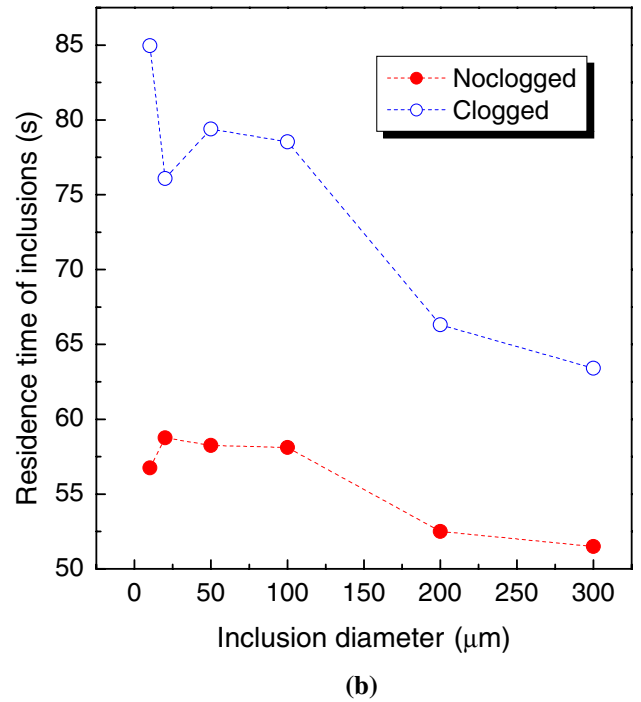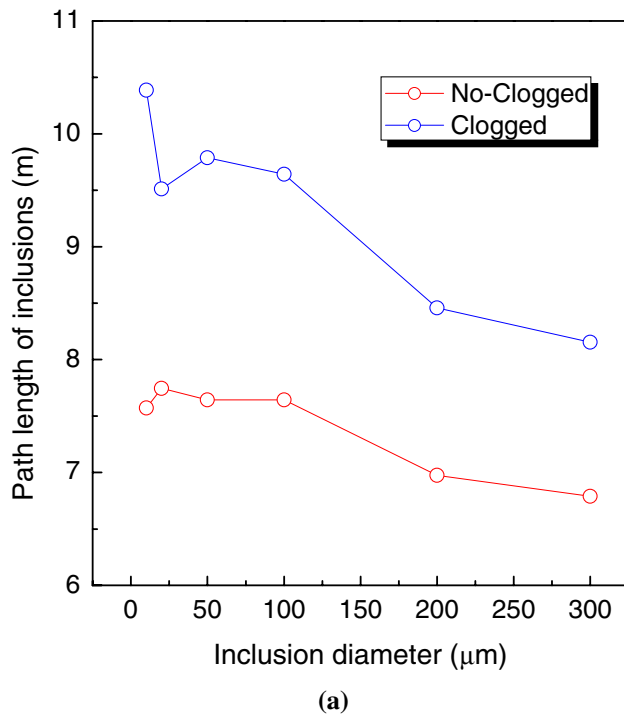
Fig. 12—3-D inclusions trajectory.

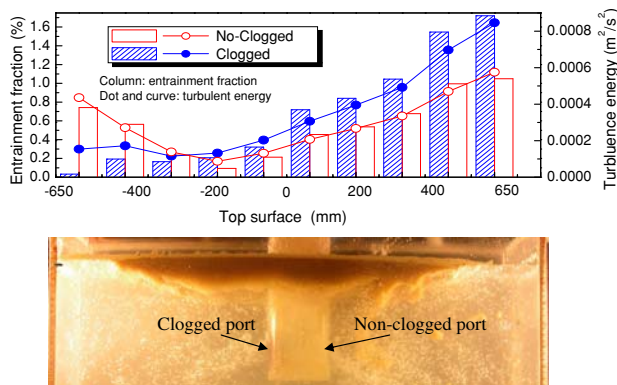Fig. 13—(*a*) Mean path lengths and (*b*) mean residence times of inclusions in the continuous casting.

Fig. 14—Entrainment fraction of the top slag: current calculation (upper) and water model result[44].
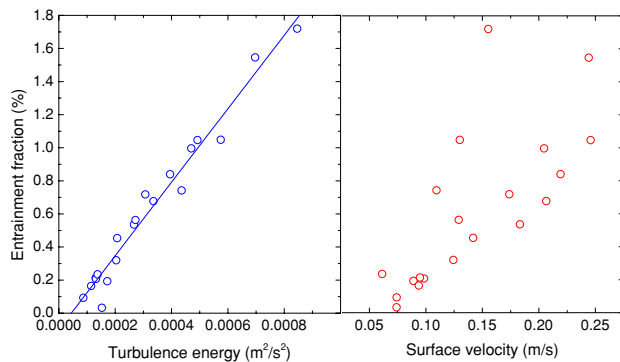

Fig. 15—Relationship between slag entrainment fraction and the turbulence energy and the surface velocity near the top surface of the mold.
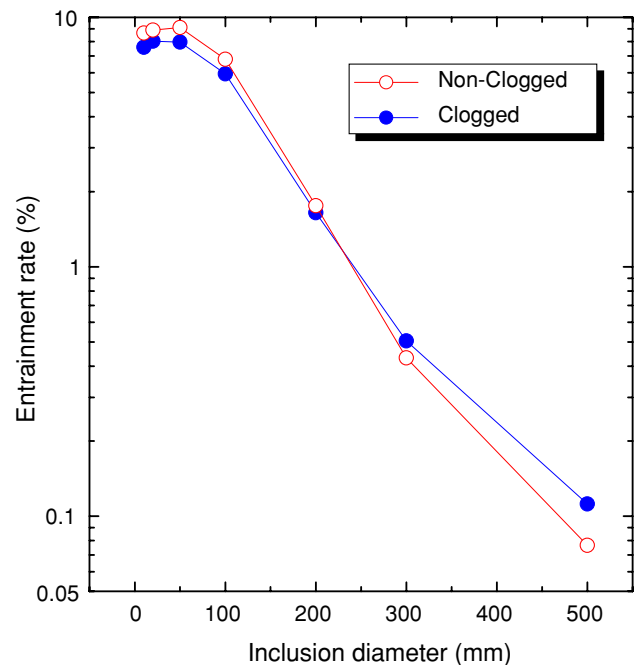

Fig. 16—Relationship between entrainment fraction and particle size.

The temperature distribution in the mold regions is shown in Figure 17; it is obvious that SEN one-sided clogging induces the asymmetrical temperature distribution in the mold region.

The heat flux at the mold walls of case A is shown in Figure 18. As explained earlier, the calculated heat flux was exported as the boundary conditions to case B. The
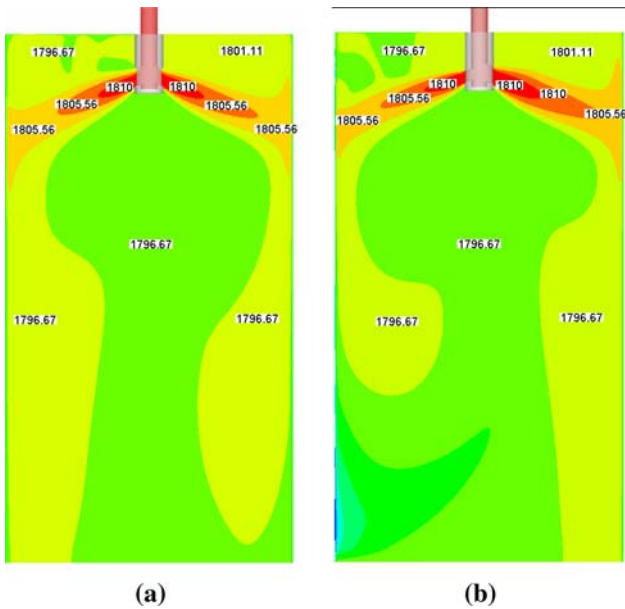
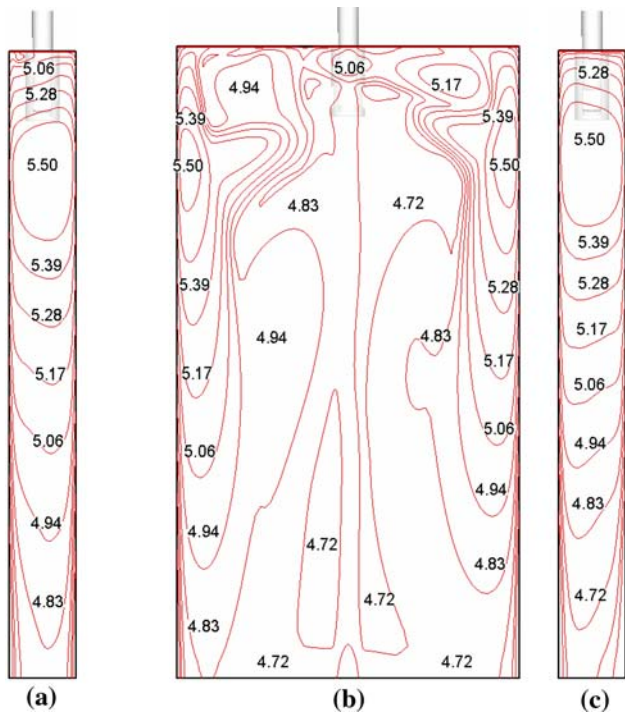Fig. 17—Temperature distribution at the center face of the mold (K): (*a*) nonclogged and (*b*) clogged.

Fig. 18—Heat flux distribution at wide and narrow faces (case A) ($\log_{10}$(-heat flux)): (*a*) left side, (*b*) wide face, and (*c*) right side.

Fig. 19—Zones with higher probability of breakout when flow became asymmetrical due to clogging.

temperature distribution on the solidifying shell with SEN clogging (case B) was then calculated. The zones with a temperature higher than the liquidus temperature are shown in Figure 19; these zones have a higher risk of breakout than do other locations. With SEN one-sided clogging, the narrow face and the corner of the nonclogged side have a high risk of breakouts.

The temperature distribution at the top surface is shown in Figure 20. At the same location, the temperature
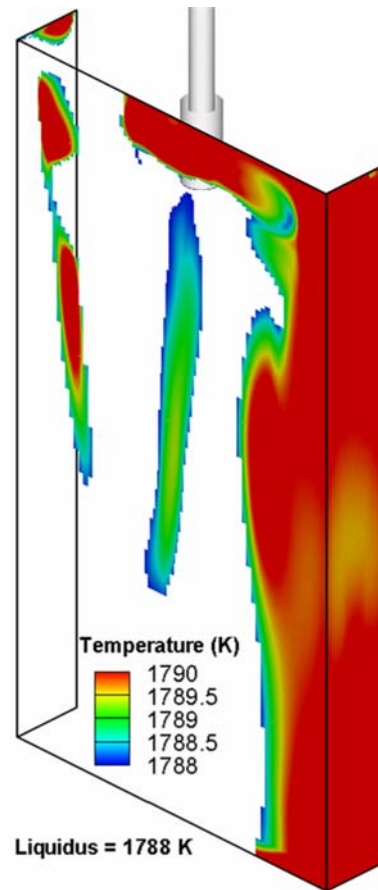
with SEN one-sided clogging is much higher than that of the nonclogging case. The mold flux at high temperature locations may be burned or pushed aside and may generate an open "eye" of the molten steel; thus, more reoxidation will occur due to the reaction with air, lowering the steel cleanliness. This phenomenon, referred to as the "jumping of the fish," has been reported in industrial practice.[35,45] By the current simulation, it is known that SEN clogging is one of the possible reasons for this phenomenon.

F. *Effect of Clogging Percentage*

Figure 21 shows the turbulent energy distribution at the center face across the mold width associated with different percentages of clogging at the SEN left port. More clogging induces a more asymmetrical flow pattern in the mold. With 100 pct clogging at the SEN left port (Figure 21(c)), the stirring at the right side (nonclogged side) of the mold is very strong, while the left side is relatively quiet. More heat will be distributed to the right narrow face than to the left one, giving a greater heat load to the right narrow face.

The liquid level across the top surface is important, because it affects the ability of the liquid flux to fill the interfacial gap between the mold and shell, which is important for heat transfer and, thereby, for the surface
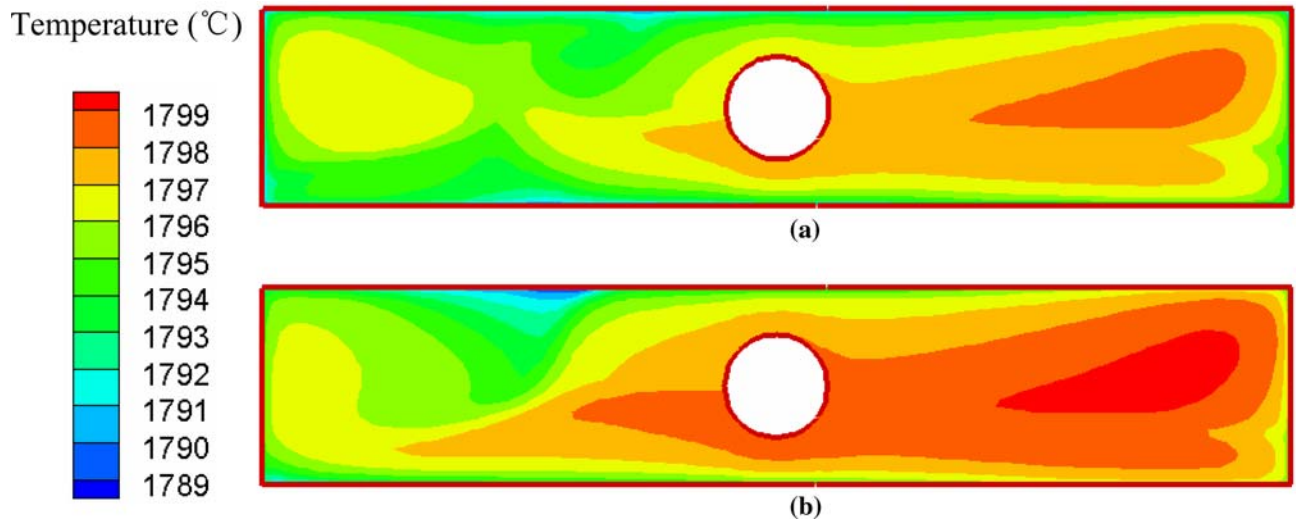
Fig. 20—Temperature distribution on the top surface: (*a*) nonclogged and (*b*) clogged.
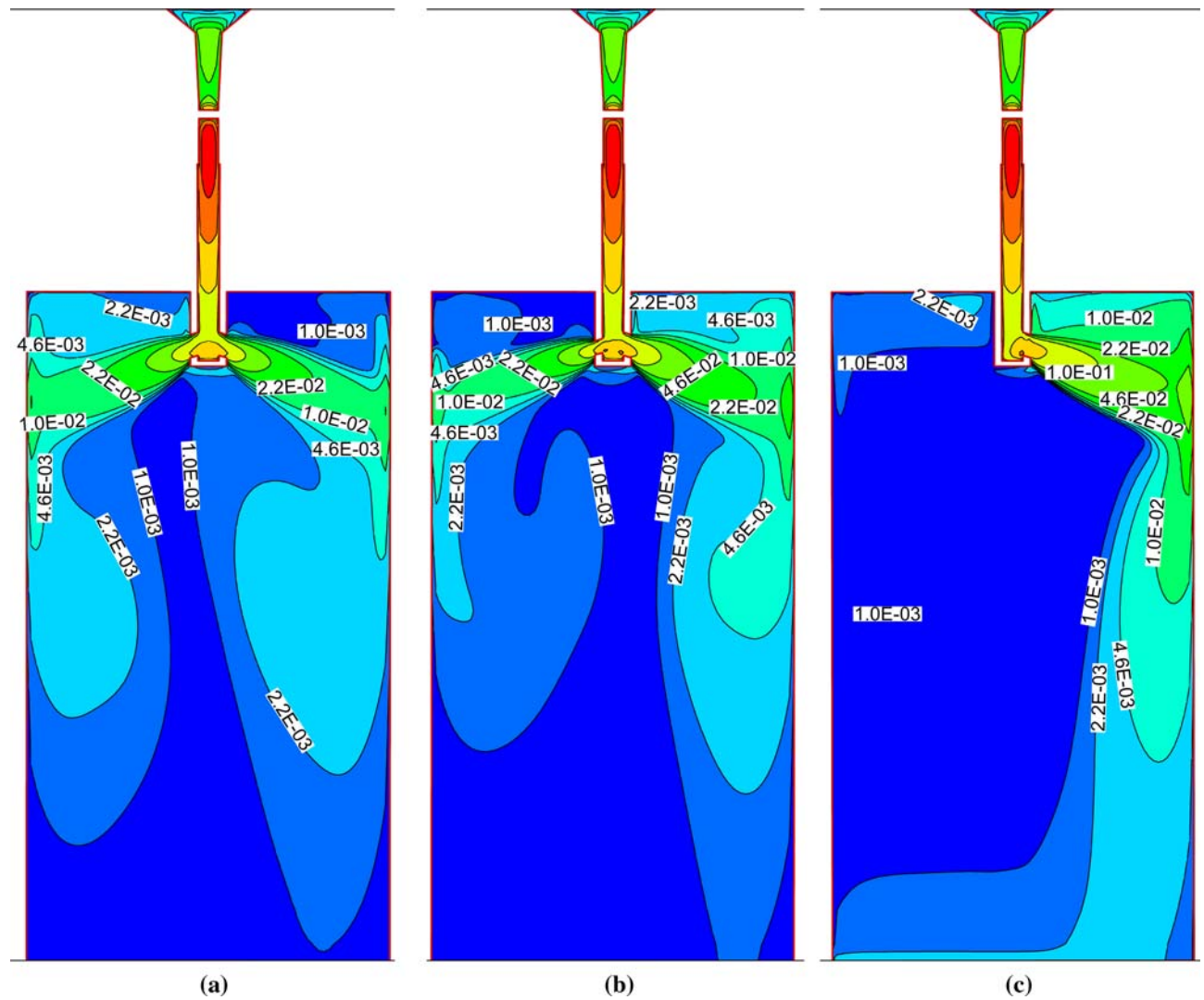

Fig. 21—Distribution of turbulence energy at the center face: (a) nonclogged; (b) SEN left port, 50 pct clogged; and (c) SEN left port, 100 pct clogged.
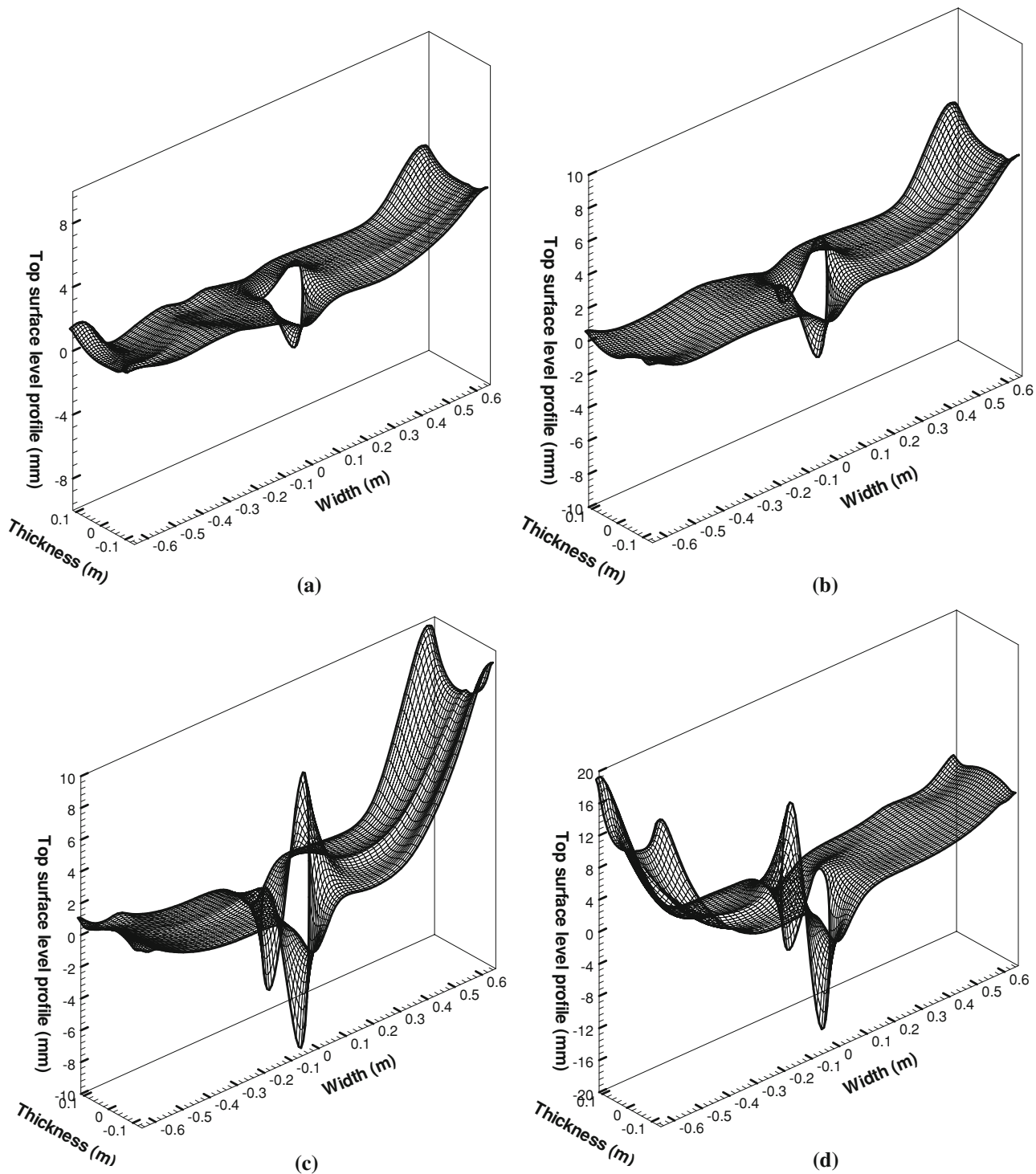
Fig. 22—Top surface level profile: (*a*) nonclogged; (*b*) SEN left port, 50 pct clogged; (*c*) SEN left port, 100 pct clogged; and (*d*) SEN left port, 50 pct clogged, and right port, 100 pct clogged.

quality of the final product. Figure 22 shows the typical top-surface levels obtained from the surface pressure results of the simulation. The top-surface liquid displacement (Δz) was estimated from a simple potential energy balance:

$$\Delta z(x, y) = \frac{p(x, y) \; - \; p_{\text{mean}}}{(\rho_l - \rho_{\text{top}})g} \qquad [5]$$

where $p(x,y)$ is the pressure at the top surface at location (x,y); p_{mean} is the mean value of the pressure across the entire top surface; ρ_l is the density of the molten steel; ρ_{top} is the density of the top slag; and g is the gravitational acceleration rate.

As indicated in Figure 22, with more clogging, the top-surface level is more asymmetrical. The nonclogged side has a higher level than does the clogged side.
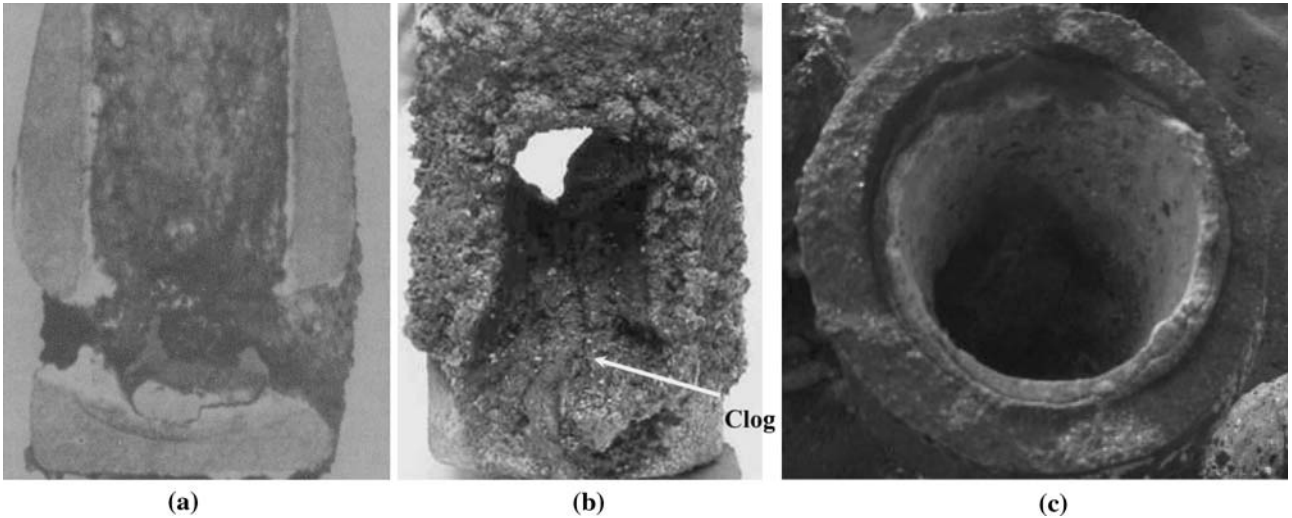
Fig. 23—Typical clogging at two-port SEN: (a) central cut of SEN,[46] (b) near outport,[22] and (c) on the inner well wall of SEN.[47]

With 50 pct clogging at the SEN left port, the highest level at the right side is approximately 6 mm; with 100 pct clogging at the SEN left port, this value increases to as high as 10 mm. A comparison of Figures 22(c) and (d) indicates that, when the open port area is smaller, the level is much higher; this is because the jet is stronger, which induces a strong recirculation at the upper roll.

G. Comparison between Numerical Modeling and Plant Data

For the current continuous-casting process, the total oxygen for the low-carbon Al-killed steel in the tundish is ~30 ppm; usually, the layer of clogged inclusions in the SEN is ~8 mm, after casting 1500 tonnes of steel. The current simulation shows that approximately 10 pct of the inclusions leaving the tundish adhere to the SEN; this is consistent with a layer of inclusions about 10-mm

thick over the entire inner wall of the SEN. The simulation agrees roughly with industrial observation.

A typical industrial observation of the attachment location of inclusions to SEN walls is shown in Figure 23;[22,46,47] this indicates that inclusions tend to adhere to the inner well wall below the slide gate and the bottom and lower side of the outports. The observation agrees well with the current numerical simulation shown in Figure 5.

The simulation indicates that, with increasing casting time, more inclusions adhere to the SEN wall, which induces more clogging; more clogging, in turn, induces more slag entrainment (Figures 14 through 16). It can be concluded that more clogging induces more serious level fluctuations and that this also induces more slag entrainment. Figure 24 shows the level fluctuation at the location of the mold top surface and the temperature fluctuation at a location inside of the mold copper plate
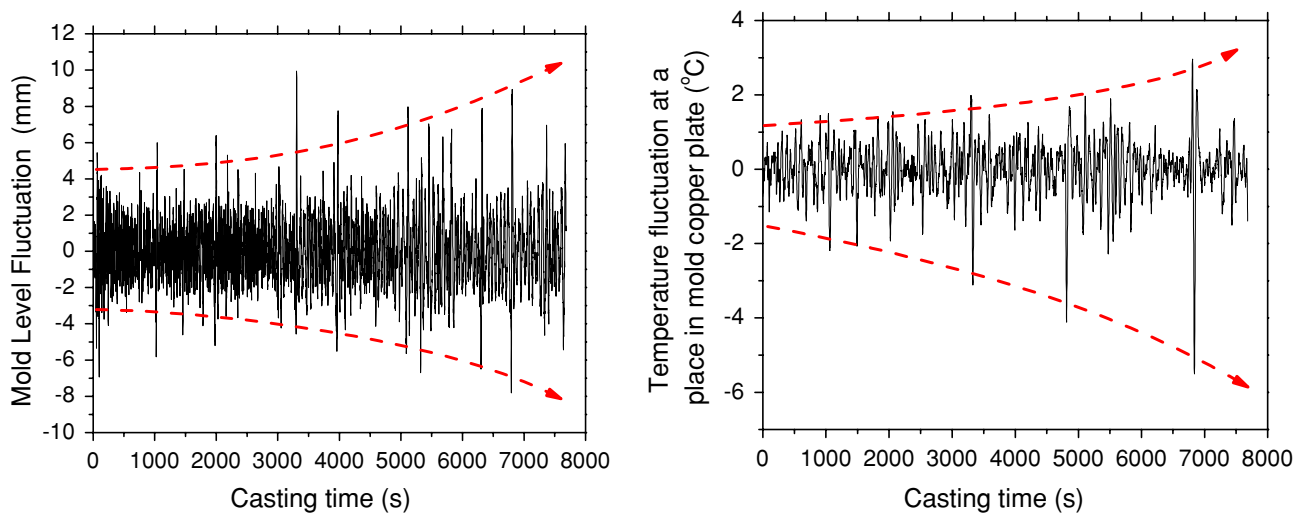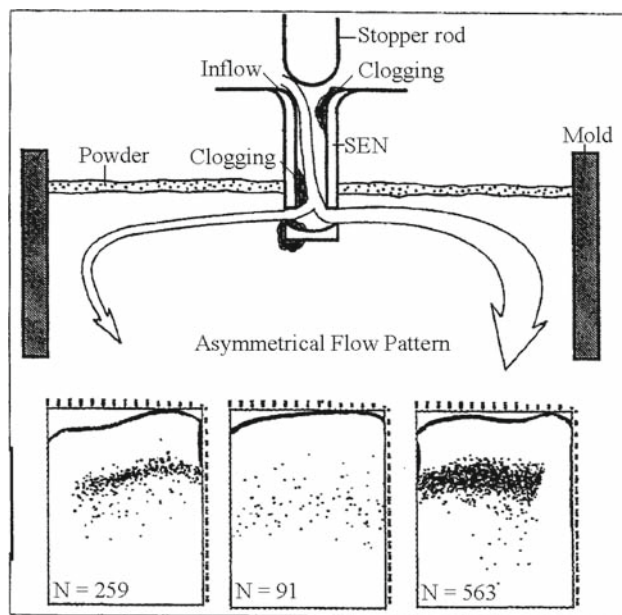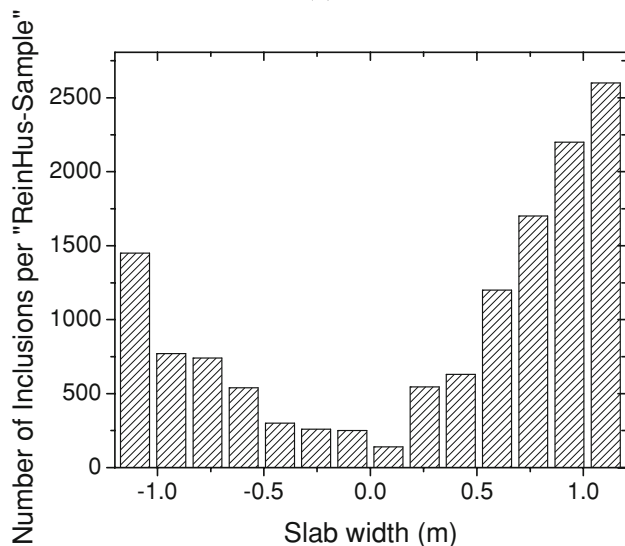

Fig. 24—Level fluctuation at a location of the mold top surface (left) and temperature fluctuation at a location inside of the mold copper plate (right).

(a)

(b)

Fig. 25—Asymmetrical contamination of continuous-cast slab due to asymmetrical flow from the SEN clogging a) (N = inclusion index by using MIDAS) (a,[48] b[49]).

for the current continuous caster; this clearly shows that, with increasing casting time, more fluctuations occur.

As shown in Figure 10, due to the asymmetrical flow pattern induced by SEN clogging, inclusion entrapment varies from side to side; more inclusions enter the steel at the nonclogged side, which hints at poorer product quality there. This agrees well with industrial measurements (Figure 25).[48,49]

Industrial measurements also verify that SEN clogging affects the heat transfer in the mold region.[50] As shown in Figure 26, with 100 pct clogging at the SEN left port, more heat will be distributed to the right narrow face than to the left one; the cooling water is

thus heated more at the right narrow face than at the left one. The simulation also indicates that the temperature inside the right side of the mold is much hotter than inside the left side. Furthermore, both the industrial measurement and the simulation indicate that, because more inclusions enter the right side, there will be more defects.

The agreement between the industrial data and the simulation indicates that the current modeling can be used to provide useful information for the industrial continuous-casting process.

V. CONCLUSIONS

The following conclusions can be drawn from this research.

1. In order to accurately simulate the fluid flow in the mold region, the SEN should be connected with the mold region and calculated together with it. In order to accurately simulate the fluid flow in the mold with nonsymmetrical SEN clogging, the whole mold region has to be calculated. In the current article, the fluid flow in a full mold region, including the tundish bottom well, upper nozzle, slide gates, SEN, mold and the vertical length of the caster, was calculated simultaneously.
2. Inclusions tend to accumulate and adhere to the SEN wall near the slide gate and the outports, and especially at the bottom and lower side of the outports. When the clogging occurred, the jet angle was 18.4 deg at the clogging side; the nonclogged side, however, had a jet angle of 24.4 deg. Without clogging, the jet angle was approximately 25 deg at both sides.
3. When the clogging occurred, the liquid steel moved from the clogging side to the normal side, which resulted in an obviously asymmetry in the mold.
4. On the nonclogged side, inclusions reached the bottom of the liquid pool more easily. With clogging, more inclusions reached the top surface of the nonclogged side. At the bottom of the liquid pool, the number of inclusions on the nonclogged side was much larger, which suggests a lower product quality at this side.
5. Larger inclusions are more easily removed. With trap boundary conditions, only <10 pct of the inclusions can be removed to the top surface, even for inclusions as large as 300 μm. Only ~3 pct of the 50-μm inclusions can be removed to the top surface.
6. Both the path length and the residence time of the small inclusions were larger than those of the larger inclusions. The path length of the inclusions is far larger than the mold region length. With SEN one-sided clogging, inclusions travel much longer before escaping from the top or entering the bottom than they do in the nonclogging case.
7. The overall slag entrainment fraction from the entire top surface for any size of slag inclusions is less than 10 pct. At the nonclogged side, the slag entrainment fraction was much higher than at the clogged side. Smaller inclusions of slag are more easily entrained
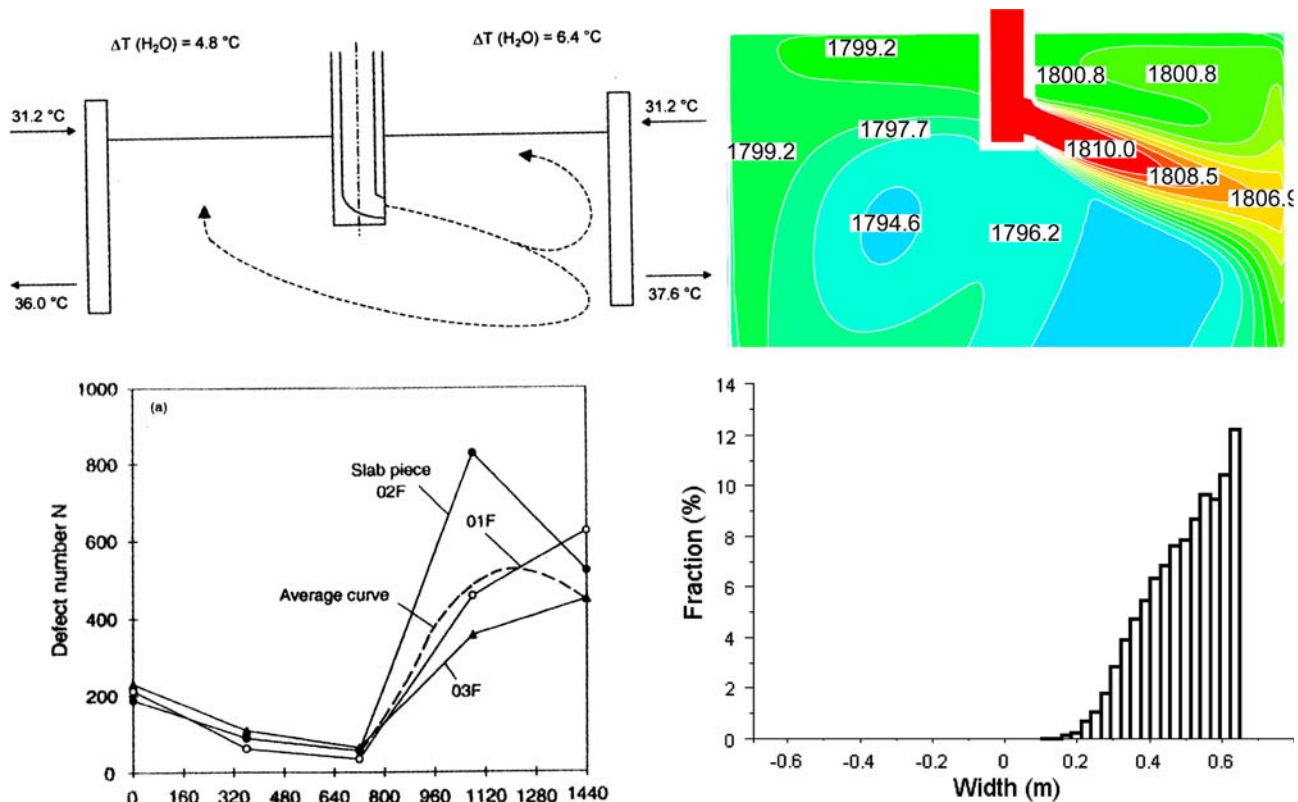
Fig. 26—Heating of mold cooling water (top figures) and cleanliness (lower figures) for a slab continuous caster. (Left is industrial measurement;[50] right is current simulation).

into the steel than are larger ones, due to their smaller buoyancy force. With SEN clogging, more > 200-μm inclusions of slag can be entrained into the steel than is the case without clogging.

8. The SEN one-sided clogging generates an asymmetrical temperature distribution in the mold. It also generates a temperature higher than the liquidus temperature at some locations of the solidified shell; this increases the risk of breakouts.

NOMENCLATURE

C_D	dimensionless drag coefficient
d_p	particle diameter (m or μm)
t	time (s)
u_{pi}	particle velocity at direction i (m/s)
u_i	velocity components of the fluid flow (m/s)
k	local level of turbulent kinetic energy (m^2/s^2)
Re_p	particle Reynolds number $(Re_p = \rho d_p |u - u_p|/\mu)$
$\bar{u}$	mean fluid phase velocity (m/s)
u'	random velocity fluctuation (m/s)
ρ	density of the molten steel (kg/m^3)
ρ_P	inclusion density (kg/m^3)
ξ	random number
μ	viscosity of the molten steel (kg/(m·s))

REFERENCES

1. Y. Vermeulen, B. Coletti, B. Blanpain, and J. Vleugels: *ISIJ Int.*, 2002, vol. 42 (11), pp. 1234–40.
2. S.K. Saxena, H. Sandberg, T. Waldenstrom, A. Persson, and S. Steensen: *Scand. J. Metall.*, 1978, vol. 7, pp. 126–33.
3. E. Lürsen: *1st Eur. Conf. on Continuous Casting*, Associazione Italiana di Metallurgia, Italy, 1991, vol. 1, pp. 1.37–1.57.
4. P.M. Benson, Q.K. Robinson, and H.K. Park: *Steelmaking Conf. Proc.*, ISS, Warrendale, PA, 1993, vol. 76, pp. 533–39.
5. M. Alavanja, R.T. Gass, R.W. Kittridge, and H.T. Tsai: *Steelmaking Conf. Proc.*, ISS, Warrendale, PA, 1995, vol. 78, pp. 415–26.
6. K.G. Rackers and B.G. Thomas: *Steelmaking Conf. Proc.*, ISS, Warrendale, PA, 1995, vol. 78, pp. 723–34.
7. H. Bai and B.G. Thomas: in *Materials Processing in the Computer Age*, V. Voller and H. Henein, eds., TMS, Warrendale, PA, 2000, vol. 3, pp. 85–99.
8. H. Bai and B.G. Thomas: *Metall. Mater. Trans. B*, 2001, vol. 32B, pp. 253–67.
9. S. Li, W. Jin, L. Zhang, X. Zuo, and Y. Wang: *Proc. AISTech 2007 Iron Steel Technology Conf. Expo.*, vol. II, AIST, Warrendale, PA, 2008, pp. 771–80.
10. E.S. Szekeres: *4th Int. Conf. Clean Steel*, The Institute of Materials, London, 1992, pp. 756–76.
11. B.G. Thomas and X. Huang: *76th Steelmaking Conf. Proc.*, ISS, Warrendale, PA, 1993, vol. 76, pp. 273–89.
12. B.G. Thomas and H. Bai: *18th Process Technology Division Conf. Proc.*, ISS, Warrendale, PA, 2001, pp. 895–912.
13. Y. Miki, H. Kitaoka, T. Sakuraya, and T. Fujii: *ISIJ Int.*, 1992, vol. 32 (1), pp. 142–49 and 1021.
14. T.B. Braun, J.F. Elliott, and M.C. Flemings: *Metall. Trans. B*, 1979, vol. 10B, pp. 171–84.
15. L. Zhang and B.G. Thomas: *Metall. Mater. Trans. B*, 2006, vol. 37B, pp. 733–61.

16. L. Zhang and B.G. Thomas: *XXIV Steelmaking Nat. Symp. Mexico*, Instituto Tecnológico de Morelia, Morelia, México, 2003, pp. 184–98.
17. F.A. Vonesh, Jr.: *Iron Steel Eng.*, 1987, vol. 64, pp. 35–39.
18. B.G. Thomas and H. Bai: *78th Steelmaking Conf. Proc.*, ISS, Warrendale, PA, 2001, pp. 895–912.
19. H. Bai and B.G. Thomas: *Metall. Mater. Trans. B*, 2001, vol. 32B, pp. 702–22.
20. L. Zhang, J. Aoki, and B.G. Thomas: *Metall. Mater. Trans. B*, 2006, vol. 37B, pp. 361–79.
21. H. Yu, G. Zhu, X. Wang, J. Zhang, and W. Wang: *J. Univ. Sci. Technol. Beijing*, 2005, vol. 12 (4), pp. 303–07.
22. R. Sambasivam: *Ironmaking and Steelmaking*, 2006, vol. 33, pp. 439–53.
23. N. Bessho, R. Yoda, H. Yamasaki, T. Fujii, T. Nozaki, and S. Takatori: *Iron Steelmaker*, 1991, vol. 18 (4), pp. 39–44.
24. I. Sawada, H. Tanaka, and I. Takigawa: *6th Int. Iron Steel Congr.*, The Iron and Steel Institute of Japan, 1990, vol. 3, pp. 334–47.
25. B.G. Thomas and L. Zhang: *ISIJ Int.*, 2001, vol. 41 (10), pp. 1181–93.
26. *FLUENT6.1 Manual*, Fluent Inc., Lebanon, NH, 2003.
27. L. Zhang and S. Taniguchi: *Int. Mater. Rev.*, 2000, vol. 45 (2), pp. 59–82.
28. M. Yemmou, M.A.A. Azouni, and P. Casses: *J. Cryst. Growth*, 1993, vol. 128 (4), pp. 1130–36.
29. J.K. Kim and P.K. Rohatgi: *Metall. Mater. Trans. B*, 1998, vol. 29A, pp. 351–75.
30. D.M. Stefanescu and A.V. Catalina: *ISIJ Int.*, 1998, vol. 38 (5), pp. 503–05.
31. Y. Ho, C. Chen, and W. Hwang: *ISIJ Int.*, 1994, vol. 34 (3), pp. 255–64.
32. B.G. Thomas and H. Zhu: *Proc. Int. Symp. Advanced Materials Technology for 21st Century*, I. Ohnaka and D. Stefanescu, eds., TMS, Warrendale, PA, 1996, pp. 197–208.
33. B. Yang and J. Su: *J. Xi'an Jiao Tong Univ.*, 1997, vol. 31 (4), pp. 67–72.
34. H. Bai and B.G. Thomas: *Metall. Mater. Trans. B*, 2001, vol. 32B, pp. 269–84.
35. L. Zhang, S. Yang, X. Wang, K. Cai, J. Li, X. Wan, and B.G. Thomas: *Metall. Mater. Trans. B*, 2007, vol. 38B, pp. 63–83.
36. B.G. Thomas, L.J. Mika, and F.M. Najjar: *Metall. Trans. B*, 1990, vol. 21B, pp. 387–400.
37. B.G. Thomas: *ISS Trans.*, 1989, vol. 16 (12), pp. 53–66.
38. S. Sivaramakrishnan, B.G. Thomas, and S.P. Vanka: in *Materials Processing in the Computer Age*, V. Voller and H. Henein, eds., TMS, Warrendale, PA, 2000, vol. 3, pp. 189–98.
39. B. G. Thomas: in *Modeling and Simulation for Casting and Solidification: Theory and Applications*, O. Yu, ed., Marcel Dekker, New York, NY, 2001, pp. 499–540.
40. B.G. Thomas, H. Bai, S. Sivaramakrishnan, and S.P. Vanka: *Int. Symp. Cutting Edge Computer Simulation of Solidification and Processes*, I. Ohnaka, ed., ISIJ, 1999, pp. 113–28.
41. X. Huang, B.G. Thomas, and F.M. Najjar: *Metall. Trans. B*, 1992, vol. 23B, pp. 339–56.
42. F.M. Najjar, D.E. Hershey, and B.G. Thomas: *4th FIDAP Users Conf.*, Fluid Dynamics International, Inc., Evanston, IL, 1991, pp. 1–55.
43. L. Zhang and W. Pluschkell: *Ironmaking and Steelmaking*, 2003, vol. 30 (2), pp. 106–10.
44. Y. Wang, G. Wen, P. Tang, H. Xu, G. Luo, Z. Chen, N. Han, and X. Ni: *Northeastern University PHD Student Forum—Metallurgy*, Northeastern University Press, Shenyang, China, 2006, p. 102.
45. J. Wei, Z. Tian, L. Zhang, K. Cai, and Y. Zhou: *Proc. AISTech 2005 Iron Steel Technol. Conf. Expo.*, AIST, Warrendale, PA, 2005, vol. II, pp. 585–92.
46. M. Byrne, T.W. Fenicle, and A.W. Cramb: *Steelmaking Conf. Proc.*, ISS, Warrendale, PA, 1985, vol. 68, pp. 451–61 and 999.
47. D.S. Kumar, T. Rajendra, A. Sarkar, A.K. Karande, and U.S. Yadav: *Ironmaking and Steelmaking*, 2007, vol. 34 (2), pp. 185–91.
48. H. Jacobi, H.-J. Ehrenberg, and K. Wunnenberg: *Stahl Eisen.*, 1998, vol. 118 (11), pp. 87–94.
49. A. Fuchs, H. Jacobi, K. Wagner, and K. Wunnenberg: *Stahl Eisen.*, 1993, vol. 113 (11), pp. 51–60.
50. H.-U. Lindenberg: *Stahl Eisen.*, 1999, vol. 119 (5), pp. 79–86.